

## Article

# Structural Controls on Mineralization within the Huanggou Gold Deposit in the Southern Mesozoic Xuefengshan Orogen, South China

Yuhua Xie <sup>1</sup>, Hua Gao <sup>1</sup>, Hua Kong <sup>2,3</sup> and Han Zheng <sup>2,3,\*</sup> 

<sup>1</sup> 301 Brigade of Hunan Nuclear Industry Geological Bureau, Changsha 410114, China; xieyh301@126.com (Y.X.); gh301@126.com (H.G.)

<sup>2</sup> School of Geosciences and Info-Physics, Central South University, Changsha 410083, China; konghua2006@126.com

<sup>3</sup> Key Laboratory of Metallogenic Prediction of Nonferrous Metals and Geological Environment Monitoring, Ministry of Education, Changsha 410083, China

\* Correspondence: hanzheng@csu.edu.cn

**Abstract:** The Mesozoic Xuefengshan Orogen (XFSO) in South China hosts abundant gold ore deposits. The XFSO records a history of polyphase tectonic deformation and the structural controls on gold mineralization are poorly understood. The recently discovered quartz-vein type Huanggou gold deposit in the southern XFSO is characterized by multiple stages of deformation and represents an excellent natural laboratory for deciphering structural controls on gold mineralization in a complex orogenic belt. A systematic structural analysis indicates that the geometry of the Huanggou gold deposit and adjacent areas mainly resulted from four stages of deformation: (1) D<sub>1</sub> top-to-the-NW sense of shearing; (2) D<sub>2</sub> SE-directed back-folding and back-thrusting; (3) D<sub>3</sub> NW–SE upright folding; and (4) D<sub>4</sub> NW–SE normal faulting and fracturing. Two sets of quartz veins are exposed in the deposit: (1) SE-dipping Au-bearing quartz veins; and (2) NW-dipping non-mineralized quartz veins. The SE-dipping Au-bearing quartz veins were likely formed by the main deformation phase of the XFSO. During D<sub>1</sub> top-to-the-NW simple shearing, these synkinematic Au-bearing quartz veins progressively evolved into sigmoidal shapes and rotated to a preferred SE-dipping orientation. Subsequently, D<sub>2</sub> SE-directed back-folding and back-thrusting resulted in the formation of synkinematic NW-dipping non-mineralized quartz veins. D<sub>3</sub> upright folding locally steepened the dips of both Au-bearing and non-mineralized quartz veins. Our results may provide new insights into the structural controls of gold mineralization in the XFSO.

**Keywords:** structural control on ore deposit; quartz-vein-type gold deposit; subsidiary fracture; shear zone; Jiangnan Orogen



**Citation:** Xie, Y.; Gao, H.; Kong, H.; Zheng, H. Structural Controls on Mineralization within the Huanggou Gold Deposit in the Southern Mesozoic Xuefengshan Orogen, South China. *Minerals* **2022**, *12*, 751. <https://doi.org/10.3390/min12060751>

Academic Editor: Alexander R.

Cruden

Received: 2 April 2022

Accepted: 2 June 2022

Published: 14 June 2022

**Publisher's Note:** MDPI stays neutral with regard to jurisdictional claims in published maps and institutional affiliations.



**Copyright:** © 2022 by the authors. Licensee MDPI, Basel, Switzerland. This article is an open access article distributed under the terms and conditions of the Creative Commons Attribution (CC BY) license (<https://creativecommons.org/licenses/by/4.0/>).

## 1. Introduction

The composite Jiangnan Orogen in South China, including the Jiuling Orogen in the east and the Xuefengshan Orogen (XFSO) in the west, represents a convergent belt between the Yangtze and Cathaysia blocks which collided during the Neoproterozoic era (Figure 1a). It subsequently underwent multistage deformations mainly in the Early Paleozoic [1–3] and Late Mesozoic [4–8] eras. The Jiangnan Orogen hosts significant gold and antimony resources and ranks as the largest antimony belt in the world and the third-largest gold belt in China [2,9]. More than 250 gold (or gold-polymetallic) deposits (or occurrences) are reported in the Jiangnan Orogen with over 970 t of total gold reserves [2,10–14]. Two dominant metallogenic epochs including the Early Paleozoic and Mesozoic eras were identified, and several Neoproterozoic deposits were discovered as well. The Early Paleozoic gold deposits are characterized by the Pingshui, Huangshan, Liulichang, Banxi, Woxi, Xiaojia, Mobin, Pingqiu, Zixi, and Pingcha deposits [15–19], and the Mesozoic gold deposits are

represented by the Mali, Yanlinsi, Wangu, Changziping, Daping, Jinjing, Fenshuiao, and Dayan deposits [17,20–25] (Figure 1a). Several genetic models such as granite intrusion-related, intracontinental reactivated, and orogenic-type were suggested for the formation of these gold deposits [1,9,24,26–28].

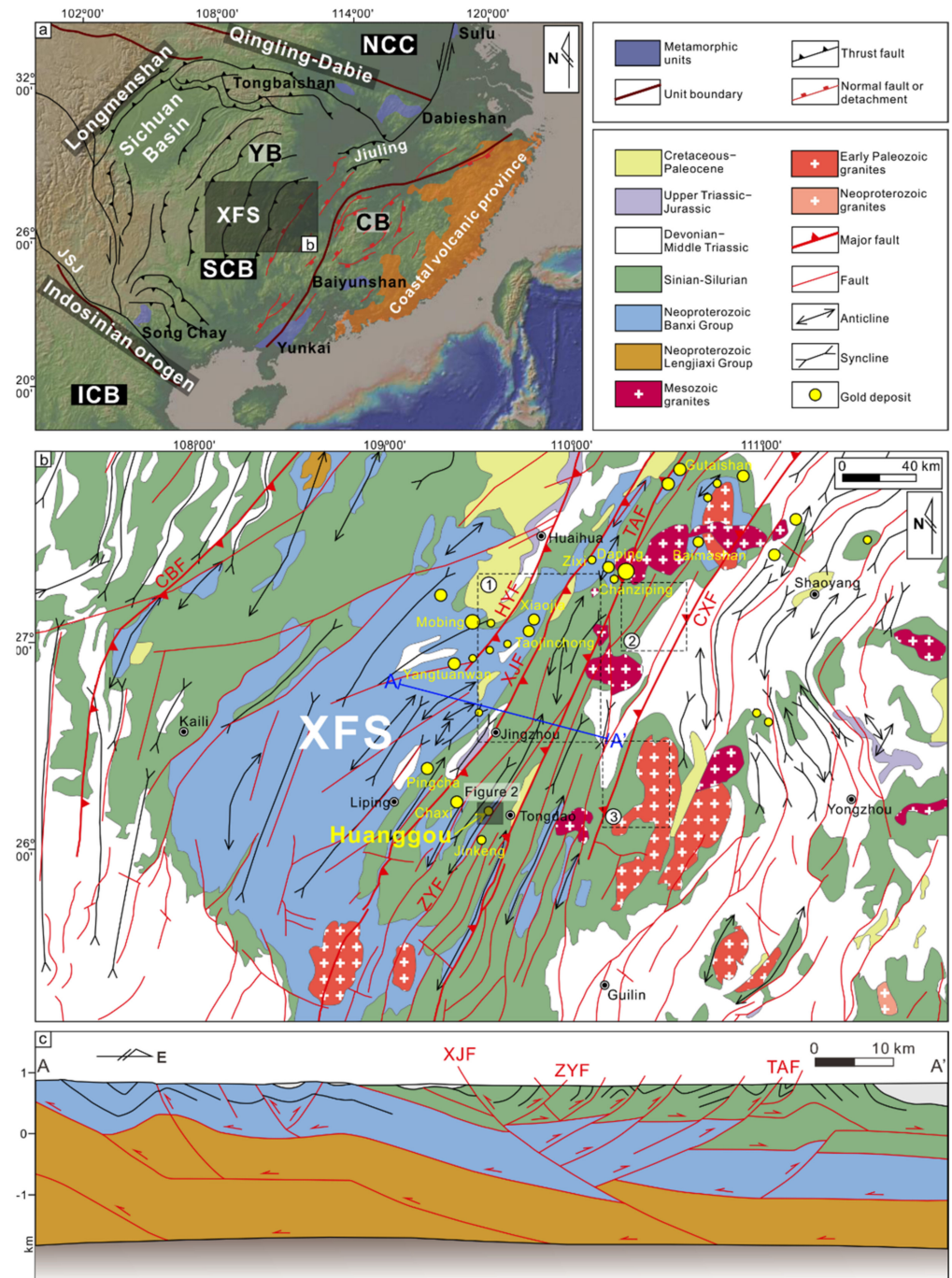


**Figure 1.** (a) Tectonic map of the South China Block and its surrounding areas. NCC: North China Craton; SCB: South China Block; YB: Yangtze Block; CB: Cathaysia Block; ICB: Indochina Block; JSJ: Jinshajiang Suture; XFS: Xuefengshan Orogen. The metamorphic units are exposed at Triassic orogens. (b) Geological map of the Xuefengshan Orogen and its adjacent regions (modified after ref. [6]). The translucent black box indicates the location of the Huanggou gold deposit. XFS: Xuefengshan Orogen. CBF: Cixi–Baojing Fault; HYF: Huaihua–Yuanling Fault; XJF: Xupu–Jingzhou Fault; ZYF: Zhaiya Fault; TAF: Tongdao–Anhua Fault; CXF: Chengbu–Xinhua Fault. (c) Cross-section A–A' shows the structural style of the southern Xuefengshan Orogen (modified after ref. [29]).

As the Jiangnan Orogen experienced several episodes of deformation, gold deposits in the orogen exhibit a complex mineralization age, ore-forming materials, and structural controls, resulting in great debates on ore deposit models. The XFSO exposes well-preserved structures associated with gold deposits and plays an excellent role in the understanding of deformation styles and tectonic patterns of the Jiangnan Orogen; however, the geometry and kinematics of the XFSO and how it controls the genesis and distribution of gold deposits are poorly understood [7,30,31] (Figure 1a,b). Furthermore, the widespread gold deposits in the Jiangnan Orogen have attracted great attention from geochemists and geochronologists for the past three decades [23,24,32–36]. In great contrast, the structural controls on gold deposits, especially in the XFSO, are seldom reported, which has greatly hindered the in-depth understanding of the mineralization of gold deposits [14,37,38]. Thus, a structural analysis on gold deposits in the XFSO is required to bring clarity to the mineralization of the orogen. This is the main motivation of this study.

The Huanggou gold deposit (Figure 1b), located in the southern XFSO, is a newly discovered quartz-vein type gold deposit. It effectively archives the polyphase deformations in the XFSO and acts as an excellent natural laboratory for deciphering the structural controls on gold mineralization in a complex orogenic belt. In this contribution, we report new structural data on the Huanggou gold deposit. Furthermore, the deformation style of each stage of deformation is decoded and the corresponding paleostress field is established. These data are then used for analyzing the structural controls on the gold mineralization of the gold deposit. Our results may provide new insights into the structural controls of gold mineralization in the XFSO.

## 2. Geological Overview of the Xuefengshan Orogen in the South China Block

### 2.1. South China Block

The South China Block (SCB) was formed by the amalgamation of the Yangtze and Cathaysia blocks in the Neoproterozoic era (Figure 1a). The collision of these two blocks is characterized by crustal shortening (Jiangnan Orogen), arc-related magmatic and sedimentary rocks (~1.0–0.90 Ga) [39–42], metamorphic rocks (~1.1–0.9 Ga) [43], and post-orogenic magmatism (~0.83–0.80 Ga) [44,45]. The Jiangnan orogeny was followed by successive sedimentation since the Late Neoproterozoic era and then modified by the Early Paleozoic (~460 to 380 Ma) intracontinental reworking [46–50]. Amphibolite to granulite facies metamorphism, migmatization, and strong deformation were archived in the Yunkai belt (Figure 1a) [3–6,47,51,52]. The termination of this intracontinental deformation is marked by a widespread Middle–Late Devonian unconformity [10,11,53].

The SCB was greatly reworked in the Triassic era (Figure 1a). In the north, the Qinling–Dabie–Sulu Orogen represents intracontinental subduction of the SCB beneath the North China Craton, which is characterized by an ultrahigh-pressure metamorphic belt [54–58]. In the southwest, the Indochina Block docked with the SCB in the Early–Middle Triassic (~245–235 Ma) and produced the Indosinian Orogen [59–62]. In the northwest, the Longmenshan Belt recorded a Triassic compressional event [63–65]. In the southeast, the subduction of the Paleo-Pacific slab under the SCB generated a wide-ranging intracontinental thrust and magmatic belt from the coast to the hinterland [4–8,49,53,66,67]. Late Triassic postorogenic magmatism and continental basin sedimentation with molasse indicate the end of Triassic tectonic events [4–8,49,53,68,69].

In the Jurassic–earliest Cretaceous, the SCB was subjected to moderate compressional deformation and some Triassic thrust belts were reactivated [70] (Figure 1a). This was followed by the Cretaceous regional extension triggered by back-arc extension of westward Paleo-Pacific subduction, although there were some alternative short compressional events [70–73]. Extensional tectonics include magmatic domes, low-angle ductile detachments, metamorphic core complexes, and (half-) graben basins, which commonly formed in two episodes at ~140–120 Ma and ~110–85 Ma, respectively [68,71,74–79].

## 2.2. Xuefengshan Orogen

The XFSO, located in the central part of the SCB, is geographically a NE-striking > 500-km-long and >1000-m-high mountain range. The XFSO is bounded by several regional-scale basins such as the Sichuan Basin in the foreland areas (Figure 1a). It is generally accepted that the orogeny of the XFSO continued to the Late Mesozoic era [80], but the Middle Triassic (~245–225 Ma) compressional deformation dominated most of the archived structural deformation of the orogen [6]. This event is marked by an extensive unconformity [4–7,62].

For the stratigraphy, the oldest sediments of the XFSO are the Neoproterozoic series, including the Lengjiaxi (Early Neoproterozoic), Banxi (Middle Neoproterozoic), and Sinian (Late Neoproterozoic) groups, from bottom to top [11]. The Lengjiaxi Group mainly consists of mica schists, quartzites, meta-sandstones, phyllites, and slates [11,81]. The unconformably overlying Banxi Group is dominated by clastic sediments such as conglomerates, sandstones, and siltstones [11,81]. The Sinian Group mainly contains tillites and limestones and the tillites from the Jiangkou and Nantuo formations are considered to represent the global glaciation events [11]. The overlying strata are Paleozoic–Early Triassic successive marine deposits, including Cambrian slaty shales, sandstones, and limestones, Ordovician limestones and argillaceous siltstones, and Silurian shales and sandstones [81]. A hiatus develops between the Middle and Late Silurian and Early Devonian eras [4–6]. A Middle Triassic compressional event widely deformed and metamorphosed (mainly greenschist facies) these pre-Triassic strata [6,8,11]. The post-orogenic deposits were fed into widely developed intracontinental basins in the XFSO [4,7,66,68].

Regarding the tectonic architecture, multistage deformations and related granitic magmatism have been identified in the XFSO in the past two decades [4–7]. It is suggested that the XFSO can be subdivided into the western and the eastern segments bounded by the NE-striking Xupu–Jingzhou Fault (Figure 1b). The fault also refers to the Main Xuefengshan Thrust in some of the literature and is interpreted as a mylonitized décollement zone [4,6,8]. The western segment consists primarily of non-metamorphic rocks and the structural pattern exhibits as km-scale box-folds with layer-slip and collapse parasitic folds. In contrast, the eastern segment contains predominantly greenschist-facies metamorphic rocks with prevalent slaty cleavages and NW- or SE-plunging lineations. NW-verging folds are well developed in this area and are accompanied by extensive back-folds and back-thrusts towards SE [4,6,8]. The eastern segment is considered to be the orogenic core of the XFSO. The Triassic compressional event is followed by a moderate Late Jurassic–earliest Cretaceous brittle dominated compressional deformation which involved thrusting and folding of Jurassic strata and locally reactivated the preexisting faults [72,80,82]. Intracontinental basins are bounded by Cretaceous normal faults or detachments and filled by thick (commonly >1 km) continental red clastic rocks with insignificant deformation [11,68,71]. Intrusive rocks are mostly exposed to the eastern segment of the XFSO (Figure 1b), including strongly deformed (ductile dominated) Early Paleozoic granitoids (~450–420 Ma), weakly deformed (brittle) Indosinian granites (~225–200 Ma), as well as several undeformed Late Mesozoic plutons (~180–120 Ma) [7].

## 2.3. Huanggou Gold Deposit

The Huanggou gold deposit is located in the eastern segment of the XFSO (Figure 1b). It lies in the northwestern limb of the NE-striking Egongling anticline and the northwest (hanging wall) of the NE-striking, NW-dipping Zhaiya Fault (Figure 1b). The regional Egongling anticline and Zhaiya Fault represent a km-scale back-fold and a back-thrust in the XFSO, respectively.

The exposed strata in the area are mainly the Mobin Formation of the Neoproterozoic Banxi Group and the Jiangkou Formation of the Lower Sinian (Figure 2a,b). Among them, the lower member of the Mobin Formation (Pt<sub>3</sub>mb<sup>1</sup>) consists largely of gray-green and gray-white medium-thick laminated medium-fine-grained metamorphic feldspar-quartz sandstones and greywackes with interbedded slates. This member is directly in contact

with the lower member of the Jiangkou Formation ( $Z_{1j}^1$ ) by the Zhaiya Fault (Figure 2a). The upper member ( $Pt_3mb^2$ ) of the Mobin Formation is dominantly gray-green slates, dark gray–black slates, and tuffaceous slates interbedded with tuffaceous siltstones. The lower member of the Jiangkou Formation ( $Z_{1j}^1$ ) mainly consists of gray-green and yellow-green gravelly sandy slates, gravelly feldspar-quartz greywackes, feldspathic-quartz sandstones interbedded with sandy slates. The upper member of the Jiangkou Formation ( $Z_{1j}^2$ ) mainly develops gray-green feldspar-quartz sandstones interbedded with slates, locally with conglomeratic quartz sandstone which contains a small number of ferrous materials (Figure 2b).

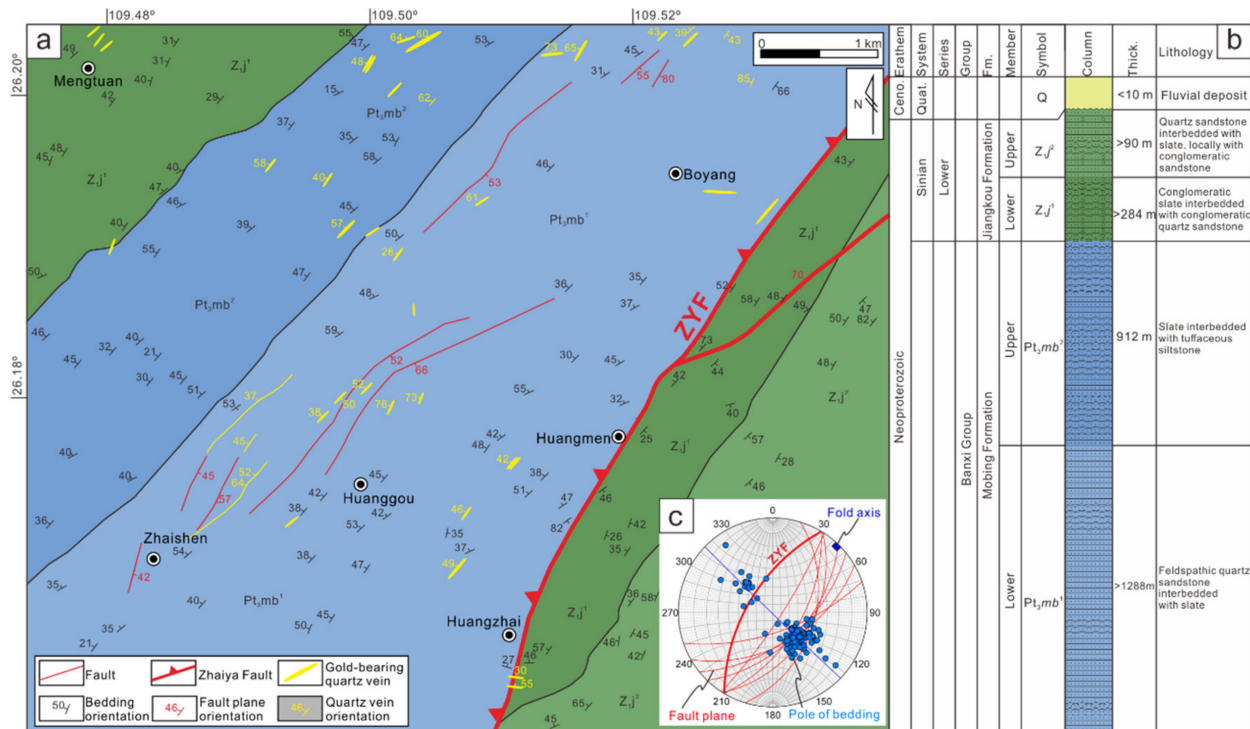


**Figure 2.** (a) Geological map of the Huanggou gold deposit. ZYF: Zhaiya Fault. (b) Stratigraphic chart of the Huanggou gold deposit. (c) Stereonet projection (equiangular; lower hemisphere) of our measurements shows the first-order NW-dipping Zhaiya Fault and higher-order SE-dipping faults. The orientations of beddings indicate the fold axis of the NE-striking regional Ergongling Fold plunges towards NE at a shallow angle.

Several fault zones have been identified in the Huanggou gold deposit (Figure 2a). These fault zones are higher-order faults and are all exposed in the hanging wall of the Zhaiya Fault (first-order fault) alongside the Mobin Formation. The fault zones are NNE–NE-striking and SE-dipping with dips ranging from 35° to 75°. The exposed lengths of the fault zones are usually between 0.7 and 2.0 km with several-meter-thick fault cores. The thickness of low-strain damage zones is commonly >100 m. The gold ores are dominantly the quartz-vein type with minor altered-rock type. Quartz vein-type ores consist of quartz–sulfide–native gold and locally quartz–carbonate–sulfide–native gold veins. Metallic minerals are dominantly native gold and subsequently pyrite and arsenopyrite, with minor chalcopyrite, sphalerite, galena, and bournonite. Visible gold is mostly produced as interstitial grains with grain sizes ranging from 0.1 to 3.0 mm. Invisible gold occurs within the crystal lattice of gold-bearing sulfides. Non-metallic minerals are mainly quartz, sericite, and chlorite. Two sets of quartz veins are identified in the deposit: (1) SE-dipping gold (Au)-bearing quartz veins and (2) NW-dipping non-mineralized quartz veins.

### 3. Methodology

A systematic structural analysis was performed to decipher the polyphase deformations of the Huanggou gold deposit and the structural controls on gold mineralization. The exposed mesoscopic structures were investigated, and various structural elements were measured in the field to obtain the orientations of beddings, fault planes, striations, cleavages, mylonitic foliations, shear bands, crenulation lineations, and stretching lineations. The geometry and kinematics of these structures are then analyzed by using stereographic projections. Then, paleostress analyses for each deformational event were performed by using the Orient software. Orientations of principal-stress axes were calculated via the classic inverse method [83].

### 4. Polyphase Deformations of the Huanggou Gold Deposit

Meso- and micro-scale structures indicate that the architecture of the Huanggou gold deposit resulted from at least four stages of deformation. (1)  $D_1$ , top-to-the-NW sense of shearing; (2)  $D_2$ , SE-directed back-folding and back-thrusting; (3)  $D_3$ , NW–SE upright folding; and (4)  $D_4$ , NW–SE normal faulting and fracturing. Detailed structural patterns of  $D_1$  to  $D_4$  are as follows.

#### 4.1. $D_1$ Top-to-the-NW Shearing

Deformation fabrics have a heterogeneous distribution with mylonitic rocks locally observed in the study area. The style of structures developed depends on the geomechanical properties of rocks. The Mobing Formation represents the exposure of a ~4-km-thick NE-striking ductile shear zone. It involves and attenuates meta-sediments and is overprinted and modified by later folds and brittle structures. The shear zone is characterized by penetrative  $D_1$  foliations ( $S_1$ ). For mylonitic rocks, S-C structures are well-developed and defined by the preferred alignment of monoclinic symmetry K-feldspar porphyroclasts and crystallized micas and quartz, indicating flow features (Figure 3a,b). Porphyroclasts are mostly  $\sigma$ -type with minor  $\delta$ -type due to their long aspect ratios. For schists, the schistosity is characterized by millimeter-scale mica- and quartz-feldspar-domains (Figure 3c). The lamination is primarily offset by shear bands (extensional crenulation cleavage) (Figure 3c). Shear bands (C-surfaces) exhibit dip directions between  $88^\circ$  and  $150^\circ$  and dips ranging from  $35^\circ$  to  $84^\circ$  (Figure 4a).  $L_1$  stretching lineation is defined by the preferential alignment of mica, quartz, and feldspar aggregates plunging towards E and SE ( $98^\circ$ – $142^\circ$ ) at angles of  $32^\circ$ – $77^\circ$  (Figure 4b). Kinematic indicators such as S-C structures, asymmetric tails of porphyroclasts, and shear bands indicate a consistent top-to-the-NW sense of shearing. These ductile structures suggest a subsimple-shearing-dominated non-coaxial deformation. For deformation mechanisms, quartz grains were commonly recrystallized by subgrain rotation (SGR), which indicates dynamic recrystallization [84–86]. Feldspars were deformed mainly by internal micro-fracturing, with minor bulging (BLG) recrystallization. According to these observations and criteria in [86], the  $D_1$  event happened under greenschist conditions. Paleostress field inversion for the  $D_1$  event yields orientations of the principal axes that indicate a NW–SE compression (Figure 4c).

#### 4.2. $D_2$ SE-Directed Back-Folding and Back-Thrusting

NW-dipping  $S_0$  surfaces (beddings or overprinting slaty cleavages) associated with long limbs of SE-verging folds can be observed in the study area (Figure 3d,e). Most folds are cylindrical folds with open to tight interlimb angles. They are inclined folds with sub-horizontal and plunging hinge lines or axes (Figure 3d,e and Figure 4d). As implied by ripple markers and load/groove casts, the  $S_0$  surfaces in the SE-limb of some anticlines are overturned. The asymmetric geometries indicate that these folds were formed by simple-shear-triggered folding. For phyllosilicate-rich rocks, pervasive SE-verging millimeter to centimeter-scale folds were formed, which constitute  $L_2$  crenulation lineations (Figure 3f).  $L_2$  crenulation lineations are NE- or SW-plunging with shallow angles (Figure 4e). On the regional scale (Figure 2a), the Mobing and Jiangkou formations consist of the km-

scale SE-verging fault-related Ergongling anticline. This fold is a cylindrical fault-related fold with a horizontal fold axis ( $44^\circ/01^\circ$ ) as illustrated by the pi-axes (Figure 2c). The NW-dipping Zhaiya Fault represents a back thrust that was formed during the D<sub>2</sub> phase and was accompanied by the SE-verging D<sub>2</sub> folds during back thrusting. Orientations of principal axes of paleostress were determined for the D<sub>2</sub> event, suggesting a NW–SE compression (Figure 4f).

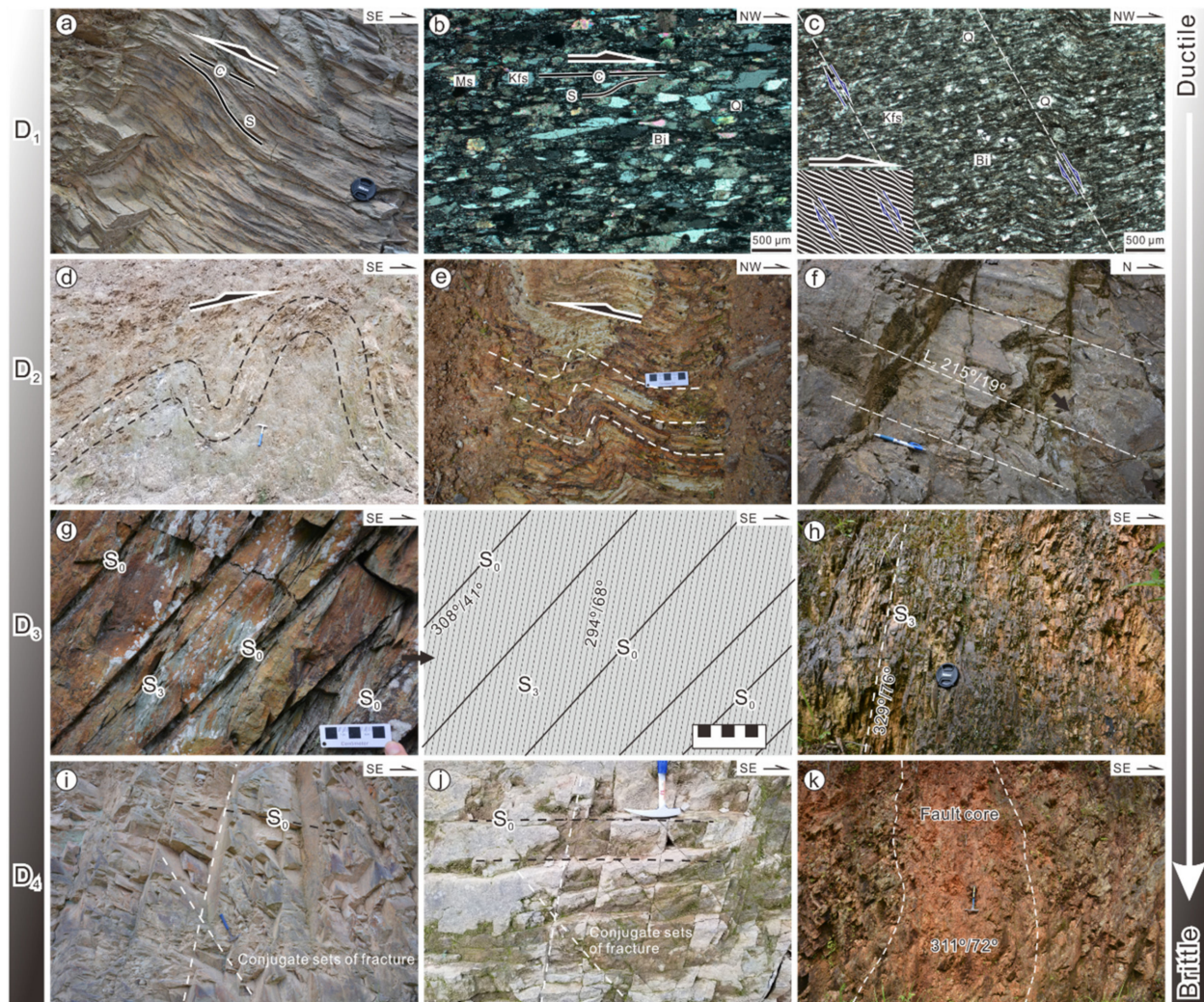


**Figure 3.** Field photographs and photomicrographs (cross-polarized) depicting main structural patterns in the Huanggou gold deposit. (a) Mesoscopic S-C structures in mylonitic rocks indicate a top-to-the-NW thrust shear sense. (b) Microscopic structures showing S-C fabrics and K-feldspar porphyroclasts. (c) Schistosity is offset by shear bands, suggesting a top-to-the-NW sense of shear. (d) SE-verging folds in slates. (e) SE-verging fold in siltstones. (f) SW-plunging crenulation lineation in phyllites. (g,h) Subvertical to vertical axial planar cleavages. (i,j) Conjugate sets of shear fractures. (k) Steep normal fault with gouges and mineralized breccias. Photomicrographs on (b,c) are XZ-plane (parallel to both the foliation and lineation). Minerals: Q: quartz; Kfs: K-feldspar; Bi: biotite; and Ms: muscovite.

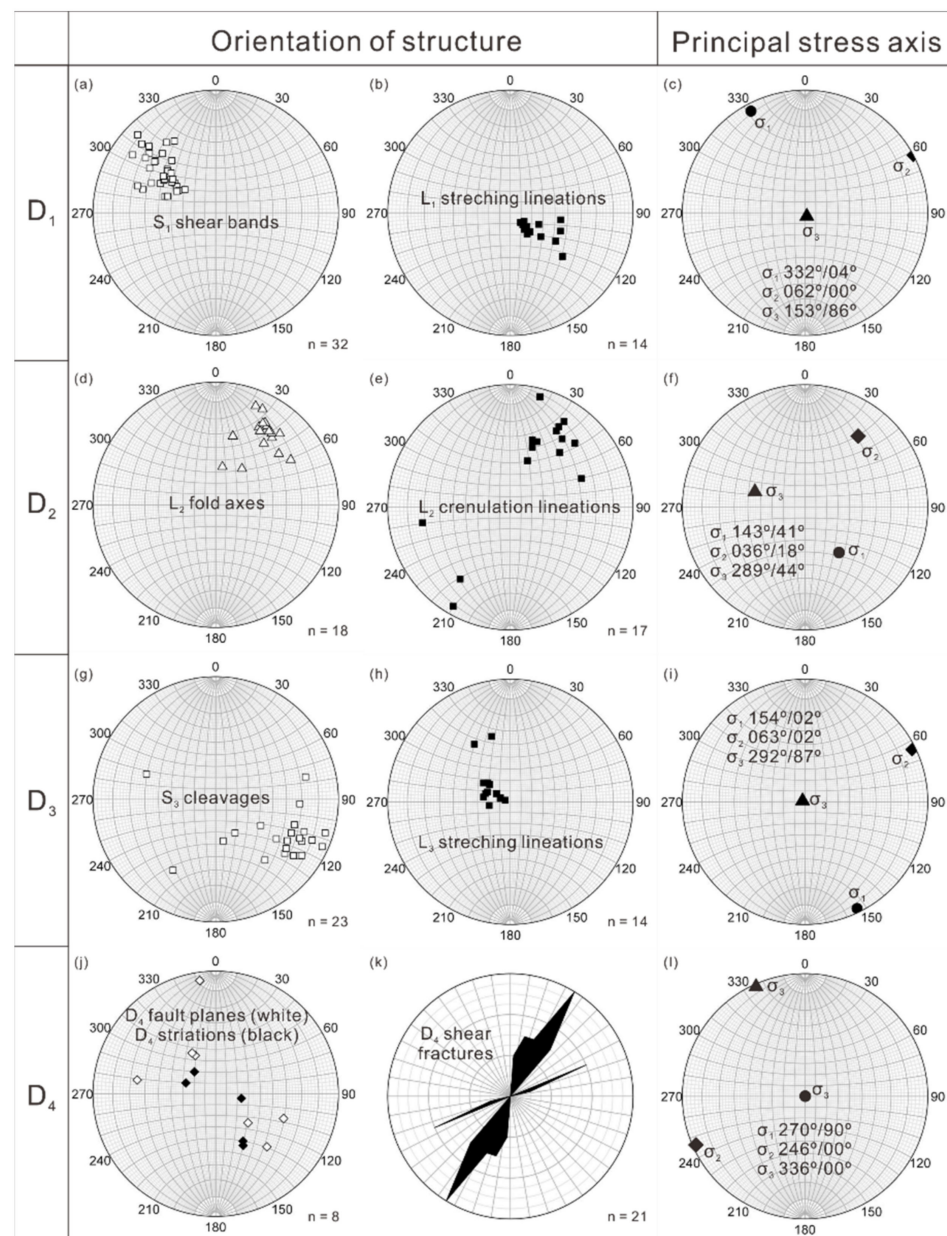


**Figure 4.** Stereonet projections (equiangular; lower hemisphere) (a–j,l) and a rose diagram (k) for orientation data of D<sub>1</sub> to D<sub>4</sub> mesoscopic structures and corresponding orientations of principal-stress axes in the Huanggou gold deposit. Poles are used for planar structures (a,g,j). Orientations of principal-stress axes were calculated by using Orient software [83].

#### 4.3. D<sub>3</sub> NW–SE Upright Folding

Phase D<sub>3</sub> is characterized by upright folds with subvertical to vertical S<sub>3</sub> axial planar cleavages and down-dip L<sub>3</sub> stretching lineations (Figure 3g,h). The contraction deformation is accommodated by pressure solution and produces axial planar cleavages. S<sub>3</sub> axial planar cleavages mainly dip towards NW (256°–350°) at 61°–87° with some SE-dipping ones (Figure 4g). L<sub>3</sub> stretching lineations mainly plunge towards NW (260°–344°) at angles of 60°–80° (Figure 4h). In the field, the orientation of S<sub>3</sub> axial planar cleavage may be seen to vary from layers with contrasting competence or viscosity and these variations reflect cleavage refraction. Sometimes it is hard to clearly distinguish if the surface represents a reworked and rotated S<sub>1</sub> foliation or a younger S<sub>3</sub> cleavage. Wulff projections of poles of S<sub>3</sub> cleavages, L<sub>3</sub> stretching lineations, and orientations of the principal-stress

axes (Figure 4i) indicate that the development of NE–SW-trending folds was triggered by NW–SE shortening.

#### 4.4. $D_4$ NW–SE Normal Faulting and Fracturing

The  $D_4$  event corresponds to brittle extension. It is characterized by pervasive conjugate sets of fractures and brittle normal faults that cross-cut  $D_1$  to  $D_3$  structures as well as  $S_0$  (Figure 3i,j,k). Brittle normal faults strike NE–SW and show brittle NW- or SE-plunging striations associated with down-dip-slip criteria (Figure 4j). The faults have steep dips and are characterized by ~0.5–2.0 m thick gouges and mineralized breccias (Figure 3k). The conjugate pairs of fractures have steep dips and exhibit straight and well-defined, finely polished fracture planes. Striations and synkinematic minerals are locally observed on the fracture planes. Rose diagrams of fractures (Figure 4k) suggest that they are bisected by the NW–SE-trending  $\sigma_3$  with an obtuse angle. These lines of evidence are kinematically consistent with normal faulting induced by NW–SE extension (Figure 4l).

### 5. Au-Bearing vs. Non-Mineralized Quartz Veins

Two sets of quartz veins are exposed in the study area: (1) SE-dipping Au-bearing quartz veins; and (2) NW-dipping non-mineralized quartz veins. These veins show an isolated arrangement pattern, and no cross-cut relationships between these two sets of veins have been found in the field (Figure 5a–i).

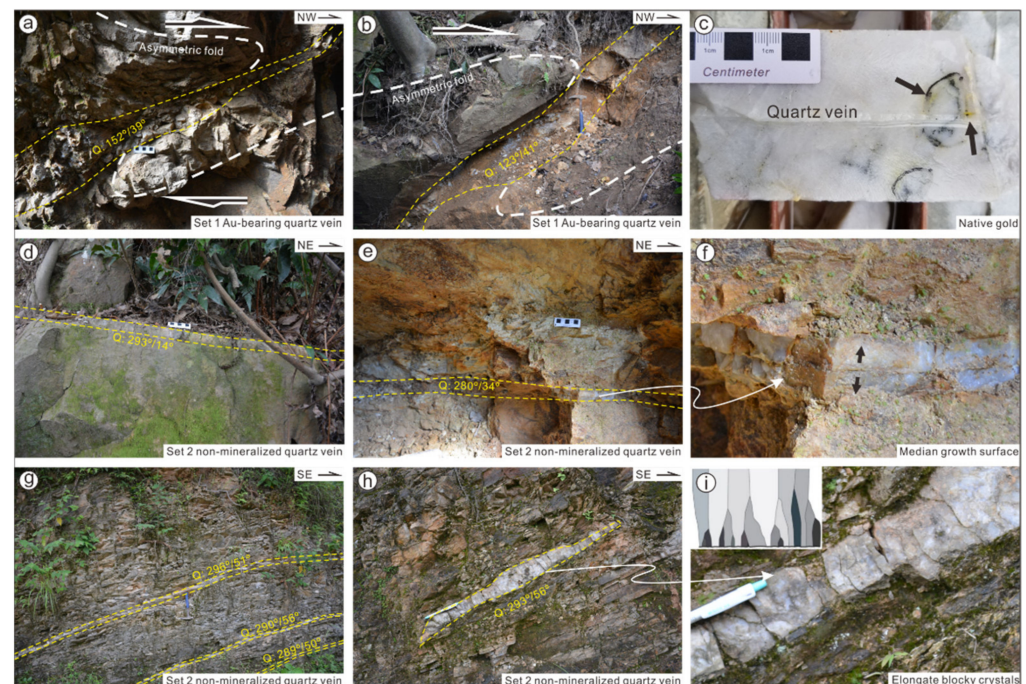


**Figure 5.** Field photographs showing structural features of two sets of quartz veins in the Huanggou gold deposit. (a,b) SE-dipping, sigmoid-shaped Au-bearing quartz veins with asymmetric folds. (c) Native gold in Au-bearing quartz vein. (d,e) NW-dipping shallow non-mineralized quartz veins. (f) Median growth surface (single crack) in quartz vein. (g,h) NW-dipping steep non-mineralized quartz veins. (i) Morphology of elongated blocky vein-filling quartz crystals.

#### 5.1. Au-Bearing Quartz Vein

Almost all Au-bearing quartz veins are located in the Neoproterozoic Mobing Formation (Figure 2a). The gold grade mainly ranges from 0.1 to 15.0 g/t up to 26.9 g/t. Most veins have a thickness between 30 and 300 cm and a length over 200 m with a maximum of ~700 m (Figures 2a and 5a,b). They are characterized by a SE-dipping orientation with dips

of  $39^{\circ}$ – $82^{\circ}$  (mainly  $40^{\circ}$ – $60^{\circ}$ ) (Figure 6a,b). These veins commonly have a median growth surface (single crack), indicating that they are most likely syntaxial veins.

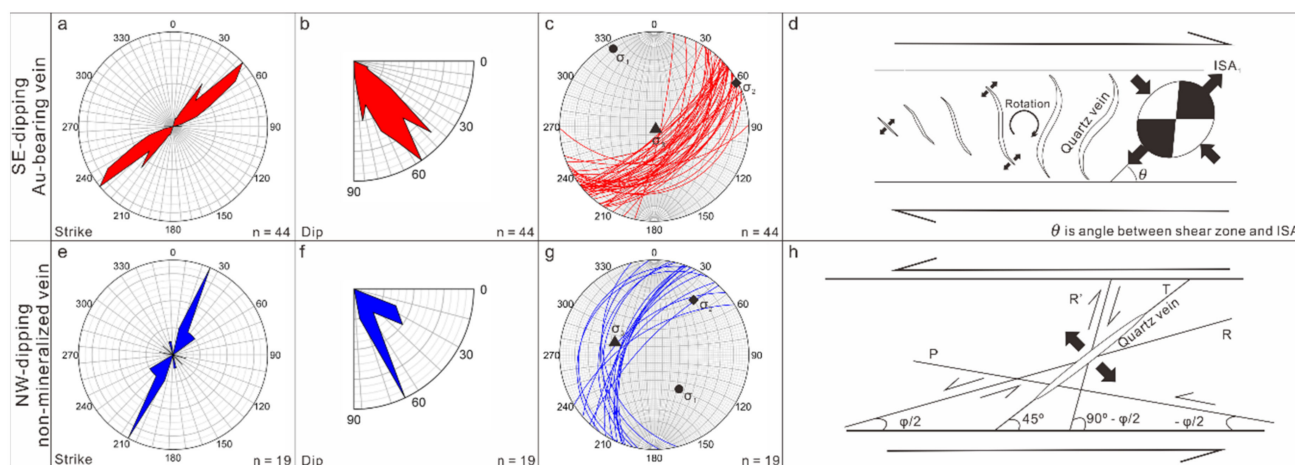


**Figure 6.** (a,b) Rose diagrams for Au-bearing quartz veins. (c) Stereonet projections (equiangular; lower hemisphere) for Au-bearing quartz veins and principal stress axes of  $D_1$ . (d) Schematics showing progressive evolution of Au-bearing quartz veins in simple shear, strain is increasing to the right. (e,f) Rose diagrams for non-mineralized quartz veins. (g) Stereonet projections (equiangular; lower hemisphere) for non-mineralized quartz veins and principal stress axes of  $D_2$ . (h) Schematics for non-mineralized quartz veins.

The Au-bearing quartz veins commonly exhibit geometries of synkinematic extension veins (Figure 5a,b). The vein tips were oriented perpendicular to the maximum instantaneous stretching direction ( $ISA_1$ ) during the associated deformation [87]. Asymmetric folds were arisen around veins, indicating a top-to-the-NW sense of shear. The central parts of the veins show some rotation (sigmoidal shape) during the progressive deformation while the tips were oriented close to  $45^{\circ}$  to the  $D_1$  C-surfaces (Figure 5a,b). Native gold is commonly observed in the veins (Figure 5c). The simple-shear-dominated opening of vein walls and folding correspond to the  $D_1$  event (Figure 6c,d). Besides, the simple-shear-controlled rotational growth of vein length and aperture (thickness) resulted in an oblique geometry between the veins and the  $\sigma_3$  of the  $D_1$  event (Figure 6c). The subsequent  $D_2$  and  $D_3$  events may also modify the orientations of the Au-bearing quartz veins to some extent.

### 5.2. Non-Mineralized Quartz Vein

Non-mineralized quartz veins are characterized by a NW-dipping orientation. They can be divided into shallow dipping and steep dipping sets. The shallow dipping set shows strikes and dips of  $280^{\circ}$ – $305^{\circ}$  /  $14^{\circ}$ – $34^{\circ}$  while the steep ones are  $288^{\circ}$ – $328^{\circ}$  /  $50^{\circ}$ – $73^{\circ}$  (Figure 6e,f). The shallow dipping set commonly has a thickness of 5–30 cm and can laterally extend tens to more than a hundred meters (Figure 5d,e). The veins are elongate blocky (long axis of vein-filling quartz crystals perpendicular to the fracture wall) with a syntaxial growth signature and oblique to the foliations or  $S_0$  surfaces of the country rocks (Figure 5f). These imply that the fractures are most likely extensional fractures (Mode I fracture) [87]. The steep dipping set typically has a small thickness of less than 10 cm with a length of several meters (Figure 5g,h). Most veins are planar with polished walls but minor veins are lens-shaped. The veins are dominantly parallel to the foliations of the surrounding rocks. The veins show elongate blocky signatures with a syntaxial origin (Figure 5i). The geometry of fractures indicates that they are possibly produced by shear fracturing (Mode II fracture) [87].

These two sets of fractures are subsidiary fractures developed along slip surfaces [87,88]. The shallow dipping set corresponds to T fractures and the steep dipping set is R or P fractures [87,88]. The elongate blocky texture of these two sets of non-mineralized veins

indicates that they were formed during the deformation. Since these fractures are brittle structures, the ductile-deformation-dominated  $D_1$  phase can be excluded. The  $D_3$  event is characterized by coaxial shortening and thus does not take responsibility for fracturing in a simple shear regime. Fractures formed by  $D_4$  extensional deformation are subvertical conjugate sets and are not reconciled with these fractures. Therefore, fractures associated with non-mineralized quartz veins are most likely formed during the  $D_2$  stage. The corresponding principal stress axes are  $\sigma_1 = 143^\circ/41^\circ$ ,  $\sigma_2 = 036^\circ/18^\circ$ , and  $\sigma_3 = 289^\circ/44^\circ$  (Figures 4f and 6g).

If the internal friction angle and the direction of simple shear are known, the ideal orientations of the subsidiary fractures can be calculated [88]. For most rocks, the coefficient of the internal friction is 0.60–0.85 [89]. Given the value of the internal friction angle ( $\Phi_F$ ) is  $35^\circ$ , and the dip of the M plane (plunge for  $\sigma_1$  of  $D_2 + \Phi_F/2$ ) is  $\beta = 58^\circ$ , the calculated dips of R ( $\Phi_F/2 + \beta$ ), R' ( $90^\circ - \Phi_F/2 + \beta$ ), T ( $45^\circ + \beta$ ) and P ( $\beta - \Phi_F/2$ ) fractures are  $75^\circ$  (synthetic),  $42^\circ$  (antithetic),  $23^\circ$  (synthetic), and  $42^\circ$  (synthetic), respectively (Figure 6h). The calculated dips of T, R, and P fractures are reconciled with most of the filed measured orientation data of NW-dipping non-mineralized quartz veins. However, dips of some veins were steepened by  $D_3$  upright folding.

## 6. Discussions

### 6.1. Timing of Polyphase Deformation

Some previous research suggests that the XFSO is primarily formed by an Early Paleozoic orogeny, as evidenced by a regional Devonian unconformity [30,31]. However, lines of evidence indicate that the dominant deformation events of the XFSO are possibly later than the Early Paleozoic era. (1) Early Paleozoic structures in the southern SCB such as those in the Wuyi–Yunkai belt [47,51,52] are not well exposed in the XFSO, related structural data are scarce as well. (2) The XFSO exhibits a low-angle ( $<20^\circ$ ) unconformity between the Devonian and its underlying sequences rather than a high-angle one [4–6]. (3) In the north and southeast of the XFSO, the archived Early Paleozoic structures are mainly south-verging open folds. These folds are km-scale undulations without obvious axial planar cleavage [5]. (4) Cleavages in the XFSO are consistently observed in rock associations from the Late Neoproterozoic to Early Triassic eras rather than developing only in pre-Devonian strata [11]. The above facts suggest that the importance of Early Paleozoic orogeny for the XFSO is overestimated and the architecture of the XFSO is mostly shaped by post-Devonian deformations.

During Neoproterozoic–Early Triassic eras, the XFSO was in a shallow sea depositional environment except for a short hiatus between the Late Silurian and Early Devonian eras [11]. Then, the Middle Triassic era represents a remarkable hiatus. The subsequent Late Triassic to Early Jurassic sedimentary sequences are characterized by clastic rocks that originated from the erosion of the XFSO. These Mesozoic sedimentary rocks are post-orogenic products fed in small-sized intramontane basins. In opposition to the pre-Middle Triassic units that are all involved in folding and thrusting, the post-Triassic series exhibit only limited brittle deformation [11,68]. It should be noted that Early Paleozoic intrusive rocks (~450–420 Ma) are widespread in the southern XFSO (Figure 1b), such as the Miaoershan and Yuechengling granitic plutons [6,90]. In the southern XFSO, these Early Paleozoic plutons were deformed by ductile shearing, which is consistent with the dominant deformation observed in the Huanggou gold deposit. Monazite U–Th–Pb<sub>tot</sub> chemical dating and SIMS U–Pb dating on zircons from micaschists indicate that the timing of ductile shearing is 243–226 Ma [5]. Furthermore, pervasive Late Triassic granites (~225–200 Ma) intruded Pre-Mesozoic strata of the XFSO (Figure 1b), such as the Baimashan batholith. These granites expose ~5600 km<sup>2</sup> in area and are lithologically two-mica granite, biotite monzonite, two-mica monzonite, and biotite-hornblende granite with lesser amounts of granodiorite and tourmaline granite [11,91]. No ductile deformation has been involved with these rocks [4,5]. Geochemical and isotopic analyses of these granitic rocks suggest that they are derived from aluminous to peraluminous felsic magma

produced by partial melting of the crust during post-orogenic extension [4,66,91–93]. These stratigraphic, tectonic, and magmatic data suggest that the Xuefengshan orogeny possibly occurred after the Early Triassic era and before ~225 Ma. This event is also marked by an extensive unconformity [4–7,62]. Wang et al. [7] reported sericite, biotite, and muscovite Ar–Ar ages of 217–195 Ma from mylonitic rocks and explained them as ductile shearing age. However, these ages may represent a cooling stage of the orogeny rather than the timing of deformation as they are younger than non-deformed, post-orogenic granites. Thus, the observed D<sub>1</sub> top-to-the-NW shearing, D<sub>2</sub> SE-directed back-folding and back-thrusting, and D<sub>3</sub> NW–SE upright folding, which shaped the dominant architecture of the Huanggou gold deposit, possibly occurred in the Middle Triassic era. The orientation data on regional bedding, foliation (cleavage and mylonitic foliation), and fold axis are highly consistent with our measured data from the Huanggou gold deposit (Figures 1b and 7). These three stages of deformation can be considered as a progressive NW–SE contractional deformation with accommodating displacement by diverse deformation styles (Figure 8a–c). Besides, the D<sub>3</sub> upright folding may provide room for the Late Triassic granite emplacement. However, the geodynamics of the Triassic orogeny is controversial. Some suggest that the collision of the SCB with the North China Craton and Indochina block takes responsible [94], while others advocate that the orogeny is related to the Paleo-Pacific subduction [5,6]. But this is beyond the scope of this paper.

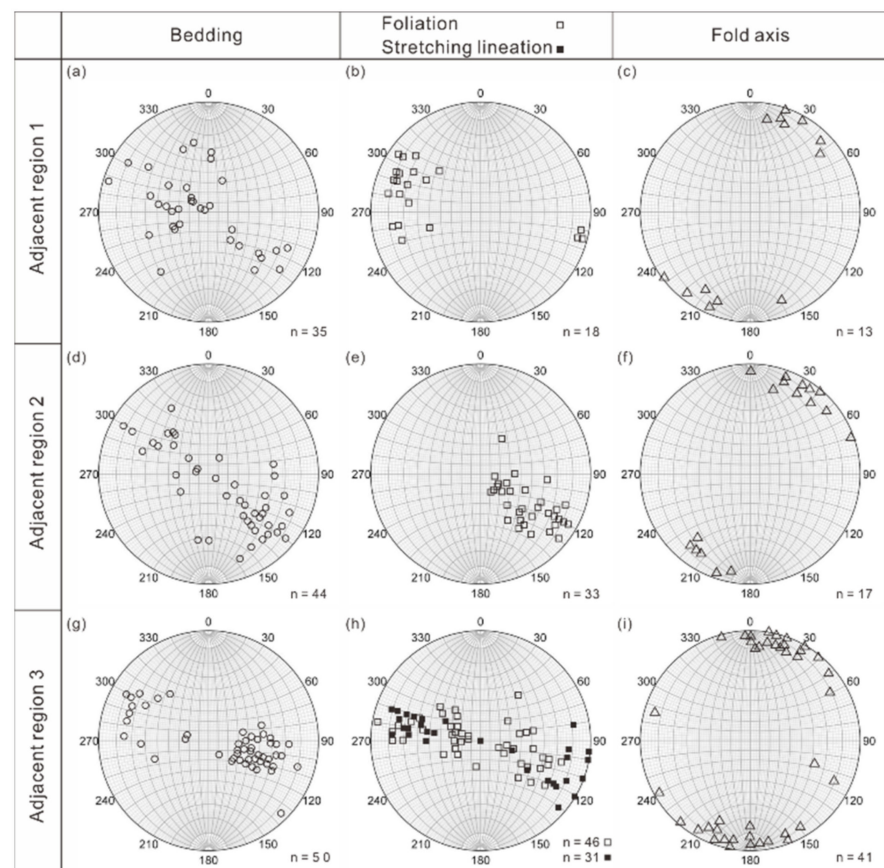


**Figure 7.** Stereonet projections (equiangular; lower hemisphere) for orientation data of bedding (a,d,g), foliations (b,e,h), stretching lineations (h), and fold axes (c,f,i) in adjacent regions of the Huanggou gold deposit. Orientation data are from [4,5] and the locations are shown in Figure 1b.

The XFSO orogeny was followed by a moderate Late Jurassic–earliest Cretaceous brittle dominated, compressional deformation which involved the thrusting and folding of Jurassic strata and locally reactivated the existing faults [72,80,82]. However, this event is subtle in the Huanggou deposit and the southern XFSO. This was followed by the

Cretaceous regional extension of the whole SCB. Widespread extensional tectonics such as magmatic domes, low-angle ductile faults, metamorphic core complexes, and (half-) graben basins were developed in two episodes of ~140–120 Ma and ~110–85 Ma ago, respectively (Figure 1a) [68,71,74–79]. The extension deformation is considered to have been triggered by back-arc extension or slab rollback of westward Paleo-Pacific subduction [49,71–73]. Thus, the D<sub>4</sub> phase of the Huanggou gold deposit can be constrained to the Cretaceous era.

### 6.2. Structural Controls on Gold Mineralization

As mentioned above, the SE-dipping Au-bearing quartz veins are most likely syn-kinematic extension veins formed by the D<sub>1</sub> event (Figure 8a). Recent H-O-S stable isotopic data [95] and typomorphic characteristics of pyrites [96] for Au-bearing quartz veins indicate that the ore-forming fluids are characterized by medium temperatures and low salinities and are metamorphic sourced with involving minor magmatic components. In consideration of the timing of deformation, we suggest that the Au-bearing quartz veins in the Huanggou gold deposit are more likely formed in the Triassic era (~243–226 Ma) [5]. However, it is hard to completely rule out the possibility of Early Paleozoic mineralization. The Early Paleozoic era (~450–420 Ma) represents an important magmatic pulse in the southern XFSO [3,90,97,98]. Besides, Early Paleozoic gold and gold–antimony deposits are pervasive in the southern XFSO and adjacent areas such as the Zixi gold deposit (425 Ma) [19] and Woxi gold–antimony deposit (420 Ma) [16]. Thus, the reliable timing of mineralization of the Huanggou gold deposit needs to be further constrained by precise isotopic dating.

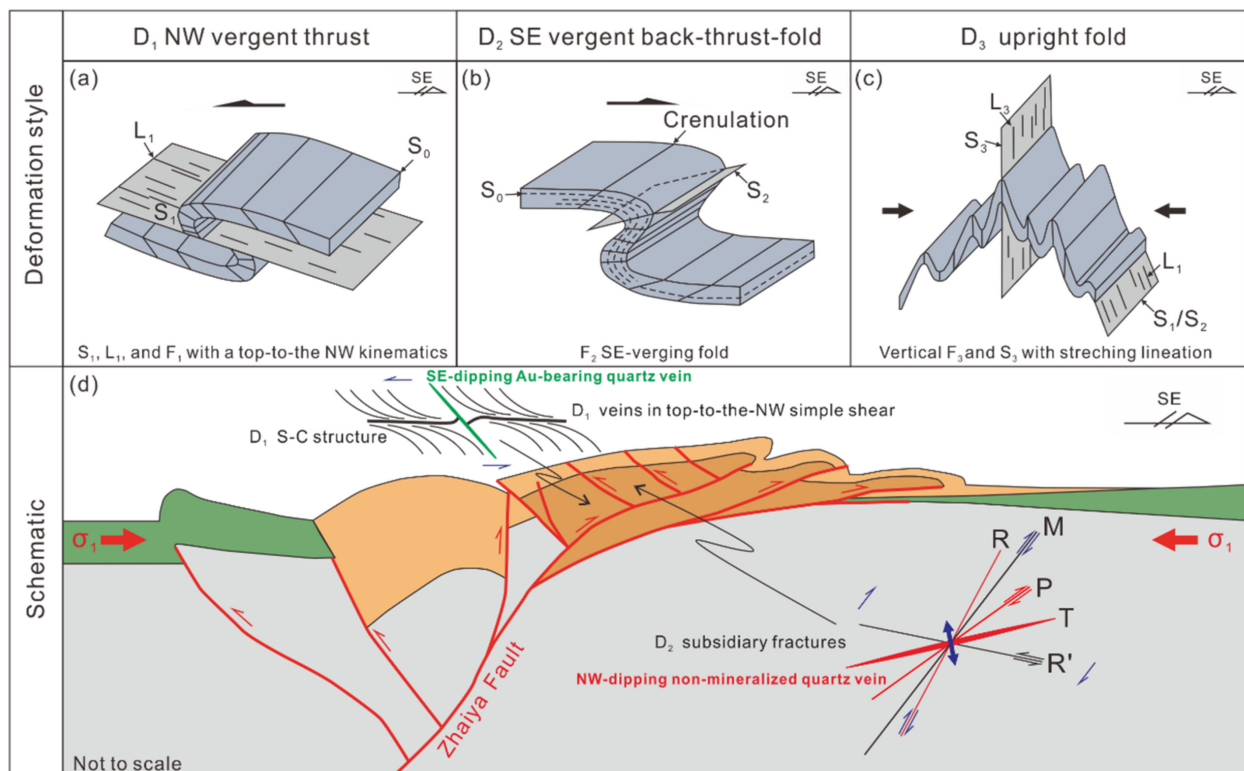


**Figure 8.** Summary of the main deformation structures with a schematic showing Au-bearing patterns. (a) D<sub>1</sub> NW vergent thrusting. (b) D<sub>2</sub> SE vergent back-thrusting-folding. (c) D<sub>3</sub> upright folding. (d) Architecture of the Huanggou gold deposit.

During the D<sub>1</sub> top-to-the-NW shearing, Au-bearing quartz veins were formed and progressively rotated to a preferred orientation through incremental strain. Most Au-bearing quartz veins are located in the Mobing Formation. This is because the rock associations of the Mobing Formation represent weak layers in comparison with the competent Jiangkou

Formation (Figure 2b). The Mobing Formation thus was subjected to strain localization during the D<sub>1</sub> deformation. Subsequently, D<sub>2</sub> SE-directed back-folding and back-thrusting along the Zhaiya Fault formed a series of subsidiary fractures and provided room for emplacement of synkinematic NW-dipping non-mineralized quartz veins (Figure 8b). This was followed by D<sub>3</sub> upright folding which may steepen the dips of both Au-bearing and non-mineralized quartz veins (Figure 8c). The brittle D<sub>4</sub> normal faulting and fracturing only had limited influence on the distribution and geometry of the quartz veins in the Huanggou gold deposit. The overprinting of these polyphase deformations of the southern XFSO shaped the final architecture of the Huanggou gold deposit (Figure 8d).

## 7. Conclusions

The polyphase structural deformations and ore-controlling styles of the Huanggou gold deposit in the southern XFSO have been deciphered by a systematic structural analysis. The main findings are as follows:

1. The geometry of the Huanggou gold deposit and adjacent areas mainly resulted from four stages of deformation: (1) D<sub>1</sub> top-to-the-NW sense of shearing; (2) D<sub>2</sub> SE-directed back-folding and back-thrusting; (3) D<sub>3</sub> NW–SE upright folding; and (4) D<sub>4</sub> NW–SE normal faulting and fracturing. The D<sub>1</sub> to D<sub>3</sub> phases, which shaped the dominant architectures of the XFSO, possibly occurred in the Middle Triassic era and can be considered as a progressive NW–SE contractional deformation with accommodating displacement by diverse deformation styles.
2. SE-dipping Au-bearing quartz veins were likely formed by the main deformation phase of the XFSO. During the D<sub>1</sub> top-to-the-NW simple shearing, these synkinematic Au-bearing quartz veins progressively evolved into sigmoidal shapes and rotated to a preferred SE-dipping orientation by means of incremental strain.
3. NW-dipping non-mineralized quartz veins are synkinematic veins. The D<sub>2</sub> SE-directed back-folding and back-thrusting produced NW-dipping non-mineralized quartz veins. The D<sub>3</sub> upright folding locally steepened the dips of both Au-bearing and non-mineralized quartz veins.

**Author Contributions:** Conceptualization, H.Z.; Data curation, Y.X. and H.K.; Formal analysis, H.G. and H.K.; Methodology, H.Z. and H.K.; Project administration, H.Z. and Y.X.; Validation, H.G. and H.K.; Writing—original draft, Y.X.; writing—review and editing, H.Z. All authors have read and agreed to the published version of the manuscript.

**Funding:** This research was funded by the Natural Science Foundation of Hunan Province (Grant 2021JJ40729) and the Hunan Nuclear Industry Geological Bureau (Grant KY2019-301-01).

**Data Availability Statement:** The data presented in this study are available on request from the corresponding author.

**Acknowledgments:** We are grateful to the academic editor and three anonymous reviewers for their helpful reviews. We thank Shefa Chen, Jishun Liu, Yong Liang, and Yixue Qin of Central South University, China, for their assistance during fieldwork. Thanks to Jonathan B. Pham for his help with the English in the manuscript.

**Conflicts of Interest:** The authors declare no conflict of interest.

## References

1. Zhao, C.; Ni, P.; Wang, G.G.; Ding, J.Y.; Chen, H.; Zhao, K.D.; Cai, Y.T.; Xu, Y.F. Geology, fluid inclusion, and isotope constraints on ore genesis of the Neoproterozoic Jinshan orogenic gold deposit, South China. *Geofluids* **2013**, *13*, 506–527. [[CrossRef](#)]
2. Deng, J.; Wang, Q.F. Gold mineralization in China: Metallogenic provinces, deposit types and tectonic framework. *Gondwana Res.* **2016**, *36*, 219–274. [[CrossRef](#)]
3. Kong, H.; Wu, J.H.; Li, H.; Chen, S.F.; Liu, B.; Wang, G. Early Paleozoic tectonic evolution of the South China Block: Constraints from geochemistry and geochronology of granitoids in Hunan Province. *Lithos* **2021**, *380*, 105891. [[CrossRef](#)]
4. Chu, Y.; Faure, M.; Lin, W.; Wang, Q. Early Mesozoic tectonics of the South China block: Insights from the Xuefengshan intracontinental orogen. *J. Asian Earth Sci.* **2012**, *61*, 199–220. [[CrossRef](#)]

5. Chu, Y.; Faure, M.; Lin, W.; Wang, Q.; Ji, W. Tectonics of the Middle Triassic intracontinental Xuefengshan Belt, South China: New insights from structural and chronological constraints on the basal décollement zone. *Int. J. Earth Sci.* **2012**, *101*, 2125–2150. [[CrossRef](#)]
6. Chu, Y.; Lin, W.; Faure, M.; Allen, M.B.; Feng, Z.T. Cretaceous exhumation of the Triassic intracontinental Xuefengshan Belt: Delayed unroofing of an orogenic plateau across the South China Block? *Tectonophysics* **2020**, *793*, 228592. [[CrossRef](#)]
7. Wang, Y.J.; Zhang, Y.H.; Fan, W.M.; Peng, T.P. Structural signatures and Ar<sup>40</sup>/Ar<sup>39</sup> geochronology of the Indosinian Xuefengshan tectonic belt, South China Block. *J. Struct. Geol.* **2005**, *27*, 985–998. [[CrossRef](#)]
8. Chu, Y.; Lin, W. Strain analysis of the Xuefengshan Belt, South China: From internal strain variation to formation of the orogenic curvature. *J. Struct. Geol.* **2018**, *116*, 131–145. [[CrossRef](#)]
9. Zhang, L.; Yang, L.Q.; Groves, D.I.; Sun, S.C.; Liu, Y.; Wang, J.Y.; Li, R.H.; Wu, S.G.; Gao, L.; Guo, J.L.; et al. An overview of timing and structural geometry of gold, gold-antimony and antimony mineralization in the Jiangnan Orogen, southern China. *Ore Geol. Rev.* **2019**, *115*, 103173. [[CrossRef](#)]
10. Jiangxi BGMR (Jiangxi Bureau of Geology and Mineral Resources). *Regional Geology of the Jiangxi Province*; Geological Publishing House: Beijing, China, 1984; p. 841. (In Chinese)
11. Hunan BGMR (Hunan Bureau of Geology and Mineral Resources). *Regional Geology of Hunan Province*; Geological Publishing House: Beijing, China, 1988; p. 722. (In Chinese)
12. Li, X.; Yi, X.; Zhu, H. Source of ore-forming fluids in Jinshan gold deposit of Dexing County: Constraints from microstructures and stable isotopes. *Miner. Deposits* **2009**, *28*, 42–52. (In Chinese with English abstract)
13. Goldfarb, R.J.; Baker, T.; Dobe, B.; Groves, D.I.; Hart, C.J.R.; Gosselin, P. Distribution, character, and genesis of gold deposits in metamorphic terranes. *Econ. Geol.* **2005**, *67*, 407–450.
14. Wen, Z.; Deng, T.; Dong, G.; Zou, F.; Xu, D.; Wang, Z.; Lin, G.; Chen, G. Study on the characters and rules of the ore-controlling structures of the Wangu gold deposit in northeastern Hunan Province. *Geotect. Metal.* **2016**, *40*, 1–14. (In Chinese with English abstract)
15. Peng, J.; Dai, T. On the mineralization epoch of the Xuefengshan gold metallogenic province. *Geol. Prospect.* **1998**, *34*, 37–41. (In Chinese)
16. Peng, J.; Hu, R.; Zhao, J.; Fu, Y.; Lin, Y. Scheelite Sm–Nd dating and quartz Ar–Ar dating for Woxi Au–Sb–W deposit, western Hunan. *Chin. Sci. Bull.* **2003**, *48*, 2640–2646. [[CrossRef](#)]
17. Wang, J.S.; Wen, H.J.; Li, C.; Ding, W.; Zhang, J.R. Re–Os isotope dating of arsenopyrite from the quartz vein-type gold deposit, Southeastern Guizhou Province, and its geological implications. *Acta Geol. Sin.* **2011**, *85*, 955–964. (In Chinese with English abstract)
18. Ni, P.; Wang, G.G.; Chen, H.; Xu, Y.F.; Guan, S.J.; Pan, J.Y.; Li, L. An Early Paleozoic orogenic gold belt along the Jiangshao Fault, South China: Evidence from fluid inclusions and Rb–Sr dating of quartz in the Huangshan and Pingshui deposits. *J. Asian Earth Sci.* **2015**, *103*, 87–102. [[CrossRef](#)]
19. Wang, C.; Shao, Y.J.; Evans, N.J.; Li, H.; Zhou, H.D.; Huang, K.X.; Liu, Z.F.; Chen, Y.; Lai, C.K.; Liu, Q.Q. Genesis of Zixi gold deposit in Xuefengshan, Jiangnan Orogen (South China): Age, geology and isotopic constraints. *Ore Geol. Rev.* **2020**, *117*, 103301. [[CrossRef](#)]
20. Ye, Y.Z.; Ye, G.S.; Zhao, G.L.; Bai, Q.R. Discussion on mineralization period of gold (silver) deposits in Huangshan district of Zhuji, Zhejiang province. *Geol. Zhejiang* **1993**, *9*, 10–14. (In Chinese with English abstract)
21. Wang, R.H.; Zhang, Q.H. Geological features and geneses of geothermal fluid leaching type gold deposits in northern Guangxi. *Guangxi Geol.* **1997**, *10*, 25–35. (In Chinese with English abstract)
22. Li, H.Q.; Wang, D.H.; Chen, F.W.; Mei, Y.P.; Cai, H. Study on chronology of the Chanziping and Daping gold deposit in Xuefeng Mountains, Hunan Province. *Acta Geol. Sin.* **2008**, *82*, 900–905. (In Chinese with English abstract)
23. Huang, C.; Fan, G.M.; Jiang, G.L.; Luo, L.; Xu, Z.L. Structural ore-controlling characteristics and electron spin resonance dating of the Yanlinsi gold deposit in northeastern Hunan Province. *Geotect. Metal.* **2012**, *36*, 76–84. (In Chinese with English abstract)
24. Deng, T.; Xu, D.; Chi, G.; Wang, Z.; Jiao, Q.; Ning, J.; Dong, G.; Zou, F. Geology, geochronology, geochemistry and ore genesis of the Wangu gold deposit in northeastern Hunan Province, Jiangnan Orogen, South China. *Ore Geol. Rev.* **2017**, *88*, 619–637. [[CrossRef](#)]
25. Xu, D.; Deng, T.; Chi, G.; Wang, Z.; Zou, F.; Zhang, J.; Zou, S.H. Gold mineralization in the Jiangnan orogenic belt of South China: Geological, geochemical and geochronological characteristics, ore deposit-type and geodynamic setting. *Ore Geol. Rev.* **2017**, *88*, 565–618. [[CrossRef](#)]
26. Zhu, Y.N.; Peng, J.T. Infrared microthermometric and noble gas isotope study of fluid inclusions in ore minerals at the Woxi orogenic Au–Sb–W deposit, western Hunan, South China. *Ore Geol. Rev.* **2015**, *65*, 55–69. [[CrossRef](#)]
27. Li, H.; Kong, H.; Zhou, Z.K.; Tindell, T.; Tang, Y.Q.; Wu, Q.H.; Xi, X.S. Genesis of the Banxi Sb deposit, South China: Constraints from wall-rock geochemistry, fluid inclusion microthermometry, Rb–Sr geochronology, and H–O–S isotopes. *Ore Geol. Rev.* **2019**, *115*, 103162. [[CrossRef](#)]
28. Li, H.; Danisik, M.; Zhou, Z.K.; Jiang, W.C.; Wu, J.H. Integrated U–Pb, Lu–Hf and (U–Th)/He analysis of zircon from the Banxi Sb deposit and its implications for the low-temperature mineralization in South China. *Geosci. Front.* **2020**, *11*, 1323–1335. [[CrossRef](#)]
29. Bai, D.Y.; Zhong, X.; Jia, P.Y.; Xiong, X. Study on the deformation in the southern Xuefeng Orogenic Belt. *Geotect. Metal.* **2014**, *142*, 512–529. (In Chinese with English abstract)

30. Qiu, Y.X.; Zhang, Y.C.; Ma, W.P. Tectonics and geological evolution of Xuefeng intra-continental Orogen, South China. *Geol. J. China Univ.* **1998**, *4*, 432–443. (In Chinese with English abstract)
31. Qiu, Y.X.; Zhang, Y.C.; Ma, W.P. *The Tectonic Nature and Evolution of Xuefeng Mountains: One Model of Formation and Evolution of Intra-Continental Orogenic Belt*; Geological Publishing House: Beijing, China, 1999. (In Chinese with English abstract)
32. Mao, J.W.; Li, H.Y.; Xu, Y.; Luo, F.T.; Li, Y.S.; Yi, Z.S.; Gu, J.N. *Geology and Genesis of the Wangu Gold Deposit in Hunan Province*; Atomic Energy Press: Beijing, China, 1997. (In Chinese with English abstract)
33. Dong, G.J.; Xu, D.R.; Wang, L.; Chen, H.H.; He, Z.L.; Fu, G.G.; Wu, J.; Wang, Z.L. Determination of mineralizing ages on gold ore deposits in the eastern Hunan province, south China and isotopic tracking on ore-forming fluids re-discussing gold ore deposit type. *Geotect. Metal.* **2008**, *32*, 482–491. (In Chinese with English abstract)
34. Han, F.B.; Chang, L.; Cai, M.H.; Liu, S.Y.; Zhang, S.Q.; Chen, Y.; Peng, Z.A.; Xu, M. Ore-forming epoch of gold deposits in northeastern Hunan. *Miner. Deposits* **2010**, *29*, 563–571. (In Chinese with English abstract)
35. Fu, S.L.; Hu, R.Z.; Yan, J.; Lan, Q.; Gao, W. The mineralization age of the Banxi Sb deposit in Xiangzhong metallogenic province in southern China. *Ore Geol. Rev.* **2019**, *112*, 103033. [[CrossRef](#)]
36. Fu, S.L.; Hu, R.Z.; Batt, G.E.; Danišik, M.; Evans, N.J.; Mi, X.F. Zircon (U-Th)/He thermochronometric constraints on the mineralization of the giant Xikuangshan Sb deposit in central Hunan, South China. *Mineral. Deposita* **2019**, *55*, 901–912. [[CrossRef](#)]
37. He, W.H.; Kang, R.H.; Liu, D.Y.; Ma, W.L.; Xie, B.W.; Hu, X.Y. The ore-controlling structure regularities and prospecting direction in Longshan Au–Sb deposit, Hunan Province. *Geol. Miner. Res. South China* **2015**, *31*, 261–267. (In Chinese with English abstract)
38. Zhang, L.J.; Shao, Y.J.; Lai, J.Q.; Shi, J.; Xu, Z.B. Analysis on ore-controlling alteration rocks and structures in the Baojingshan–Jinkengchong gold deposit, Hunan. *Miner. Explor.* **2015**, *6*, 245–253. (In Chinese with English abstract)
39. Li, X.H. U–Pb zircon ages of granites from the southern margin of the Yangtze Block: Timing of Neoproterozoic Jinning Orogeny in SE China and implications for Rodinia assembly. *Precambrian Res.* **1999**, *97*, 43–57. [[CrossRef](#)]
40. Li, X.H.; Li, W.X.; Li, Z.X.; Lo, C.H.; Wang, J.; Ye, M.F.; Yang, Y.H. Amalgamation between the Yangtze and Cathaysia Blocks in South China: Constraints from SHRIMP U–Pb zircon ages, geochemistry and Nd–Hf isotopes of the Shuangxiwu volcanic rocks. *Precambrian Res.* **2009**, *174*, 117–128. [[CrossRef](#)]
41. Wang, W.; Zhou, M.F.; Yan, D.P.; Li, L.; John, M. Detrital zircon record of Neoproterozoic active-margin sedimentation in the eastern Jiangnan Orogen, South China. *Precambrian Res.* **2013**, *235*, 1–19. [[CrossRef](#)]
42. Wang, W.; Zhou, M.F.; Zhao, J.H.; Pandit, M.; Zheng, J.P.; Liu, Z.R. Neoproterozoic active continental margin in the southeastern Yangtze Block of South China: Evidence from the ca. 830–810 Ma sedimentary strata. *Sediment. Geol.* **2016**, *342*, 254–267. [[CrossRef](#)]
43. Li, Z.X.; Wartho, J.A.; Occhipinti, S.; Zhang, C.L.; Li, X.H.; Wang, J.; Bao, C.M. Early history of the eastern Sibao Orogen (South China) during the assembly of Rodinia: New mica Ar-40/Ar-39 dating and SHRIMP U–Pb detrital zircon provenance constraints. *Precambrian Res.* **2007**, *159*, 79–94. [[CrossRef](#)]
44. Wang, X.L.; Zhou, J.C.; Qiu, J.S.; Zhang, W.L.; Liu, X.M.; Zhang, G.L. LA-ICP-MS U–Pb zircon geochronology of the Neoproterozoic igneous rocks from Northern Guangxi, South China: Implications for tectonic evolution. *Precambrian Res.* **2006**, *145*, 111–130. [[CrossRef](#)]
45. Zheng, Y.F.; Gong, B.; Zhao, Z.F.; Wu, Y.B.; Chen, F.K. Zircon U–Pb age and O isotope evidence for Neoproterozoic low-O<sub>2</sub> magmatism during supercontinental rifting in South China: Implications for the snowball Earth event. *Am. J. Sci.* **2008**, *308*, 484–516. [[CrossRef](#)]
46. Wang, J.; Li, Z.X. History of Neoproterozoic rift basins in South China: Implications for Rodinia break-up. *Precambrian Res.* **2003**, *122*, 141–158. [[CrossRef](#)]
47. Faure, M.; Shu, L.; Wang, B.; Charvet, J.; Choulet, F.; Monié, P. Intracontinental subduction: A possible mechanism for the Early Palaeozoic Orogen of SE China. *Terra Nova* **2009**, *21*, 360–368. [[CrossRef](#)]
48. Charvet, J.; Shu, L.; Faure, M.; Choulet, F.; Wang, B.; Lu, H.; Le Breton, N. Structural development of the lower Paleozoic belt of South China: Genesis of an intracontinental orogen. *J. Asian Earth Sci.* **2010**, *39*, 309–330. [[CrossRef](#)]
49. Li, Z.X.; Li, X.H.; Wartho, J.A.; Clark, C.; Li, W.X.; Zhang, C.L.; Bao, C. Magmatic and metamorphic events during the early Paleozoic Wuyi–Yunkai orogeny, southeastern South China: New age constraints and pressure–temperature conditions. *Geol. Soc. Am. Bull.* **2010**, *122*, 772–793. [[CrossRef](#)]
50. Chu, Y.; Lin, W. Phanerozoic polyorogenic deformation in southern Jiuling Massif, northern South China block: Constraints from structural analysis and geochronology. *J. Asian Earth Sci.* **2014**, *86*, 117–130. [[CrossRef](#)]
51. Lin, W.; Wang, Q.; Chen, K. Phanerozoic tectonics of south China block: New insights from the polyphase deformation in the Yunkai massif. *Tectonics* **2008**, *27*, TC6004. [[CrossRef](#)]
52. Shu, L.S.; Jahn, B.M.; Charvet, J.; Santosh, M.; Wang, B.; Xu, X.S.; Jiang, S.Y. Intraplate tectono-magmatism in the Cathaysia Block (South China): Evidence from stratigraphic, structural, geochemical and geochronological investigations. *Am. J. Sci.* **2014**, *314*, 154–186. [[CrossRef](#)]
53. Shu, L.S.; Wang, B.; Cawood, P.A.; Santosh, M.; Xu, Z.Q. Early Paleozoic and Early Mesozoic intraplate tectonic and magmatic events in the Cathaysia Block, South China. *Tectonics* **2015**, *34*, 1600–1621. [[CrossRef](#)]
54. Hacker, B.R.; Ratschbacher, L.; Webb, L.; McWilliams, M.O.; Ireland, T.; Calvert, A.; Dong, S.W.; Wenk, H.R.; Chateigner, D. Exhumation of ultrahigh-pressure continental crust in east central China: Late Triassic–Early Jurassic tectonic unroofing. *J. Geophys. Res.* **2000**, *105*, 13339–13364. [[CrossRef](#)]

55. Meng, Q.R.; Zhang, G.W. Geologic framework and tectonic evolution of the Qinling orogen, central China. *Tectonophysics* **2000**, *323*, 183–196. [[CrossRef](#)]
56. Ratschbacher, L.; Hacker, B.R.; Webb, L.E.; McWilliams, M.; Ireland, T.; Dong, S.; Calvert, A.; Chateigner, D.; Wenk, H.R. Exhumation of the ultrahigh-pressure continental crust in east central China: Cretaceous and Cenozoic unroofing and the Tanlu fault. *J. Geophys. Res.* **2000**, *105*, 13303–13338. [[CrossRef](#)]
57. Faure, M.; Lin, W.; Le Breton, N. Where is the North China-South China block boundary in eastern China? *Geology* **2001**, *29*, 119–122. [[CrossRef](#)]
58. Faure, M.; Lin, W.; Scharer, U.; Shu, L.S.; Sun, Y.; Arnaud, N. Continental subduction and exhumation of UHP rocks. Structural and geochronological insights from the Dabieshan (East China). *Lithos* **2003**, *70*, 213–241. [[CrossRef](#)]
59. Lepvrier, C.; Maluski, H.; Van Tich, V.; Leyreloup, A.; Truong Thi, P.; Van Vuong, N. The Early Triassic Indosinian orogeny in Vietnam (Truong Son Belt and Kontum Massif); implications for the geodynamic evolution of Indochina. *Tectonophysics* **2004**, *393*, 87–118. [[CrossRef](#)]
60. Lepvrier, C.; Faure, M.; Van, V.N.; Vu, T.V.; Lin, W.; Trong, T.T.; Hoa, P.T. Northdirected Triassic nappes in Northeastern Vietnam (East Bac Bo). *J. Asian Earth Sci.* **2011**, *41*, 56–68. [[CrossRef](#)]
61. Faure, M.; Lepvrier, C.; Nguyen, V.V.; Vu, T.V.; Lin, W.; Chen, Z. The South China block-Indochina collision: Where, when, and how? *J. Asian Earth Sci.* **2014**, *79*, 260–274. [[CrossRef](#)]
62. Faure, M.; Lin, W.; Chu, Y.; Lepvrier, C. Triassic tectonics of the Ailaoshan Belt (SW China): Early Triassic collision between the South China and Indochina Blocks, and Middle Triassic intracontinental shearing. *Tectonophysics* **2016**, *683*, 27–42. [[CrossRef](#)]
63. Harrowfield, M.J.; Wilson, C.J.L. Indosinian deformation of the Songpan Ganze Fold Belt, northeast Tibetan Plateau. *J. Struct. Geol.* **2005**, *27*, 101–117. [[CrossRef](#)]
64. Yan, D.P.; Zhou, M.F.; Li, S.B.; Wei, G.Q. Structural and geochronological constraints on the Mesozoic-Cenozoic tectonic evolution of the Longmen Shan thrust belt, eastern Tibetan Plateau. *Tectonics* **2011**, *30*, TC6005. [[CrossRef](#)]
65. Xue, Z.; Martelet, G.; Lin, W.; Faure, M.; Chen, Y.; Wei, W.; Li, S.; Wang, Q. Mesozoic crustal thickening of the Longmenshan Belt (NE Tibet, China) by imbrication of basement slices: Insights from structural analysis, petrofabric and magnetic fabric studies, and gravity modeling. *Tectonics* **2017**, *36*, 3110–3134. [[CrossRef](#)]
66. Li, Z.X.; Li, X.H. Formation of the 1300-km-wide intracontinental orogen and postorogenic magmatic province in Mesozoic South China: A flat-slab subduction model. *Geology* **2007**, *35*, 179–182. [[CrossRef](#)]
67. Xu, X.B.; Zhang, Y.Q.; Shu, L.S.; Jia, D. La-ICP-MS U-Pb and  $^{40}\text{Ar}/^{39}\text{Ar}$  geochronology of the sheared metamorphic rocks in the Wuyishan: Constraints on the timing of Early Paleozoic and Early Mesozoic tectono-thermal events in SE China. *Tectonophysics* **2011**, *501*, 71–86.
68. Shu, L.S.; Zhou, X.M.; Deng, P.; Wang, B.; Jiang, S.Y.; Yu, J.H.; Zhao, X.X. Mesozoic tectonic evolution of the Southeast China Block: New insights from basin analysis. *J. Asian Earth Sci.* **2009**, *34*, 376–391. [[CrossRef](#)]
69. Qiu, L.; Yan, D.-P.; Yang, W.-X.; Wang, J.; Tang, X.; Ariser, S. Early to Middle Triassic sedimentary records in the Youjiang Basin, South China: Implications for Indosinian orogenesis. *J. Asian Earth Sci.* **2017**, *141*, 125–139. [[CrossRef](#)]
70. Li, J.; Dong, S.; Cawood, P.A.; Zhao, G.; Johnston, S.T.; Zhang, Y.; Xin, Y. An Andean-type retro-arc foreland system beneath northwest South China revealed by SINOPROBE profiling. *Earth Planet. Sci. Lett.* **2018**, *490*, 170–179. [[CrossRef](#)]
71. Li, J.; Zhang, Y.; Dong, S.; Johnston, S.T. Cretaceous tectonic evolution of South China: A preliminary synthesis. *Earth Sci. Rev.* **2014**, *134*, 98–136. [[CrossRef](#)]
72. Li, Z.X.; Li, X.H.; Chung, S.L.; Lo, C.H.; Xu, X.; Li, W.X. Magmatic switch-on and switch-off along the South China continental margin since the Permian: Transition from an Andean-type to a Western Pacific-type plate boundary. *Tectonophysics* **2012**, *532–535*, 271–290. [[CrossRef](#)]
73. Jiang, X.Y.; Li, X.H.; Collins, W.J.; Huang, H.Q. U-Pb age and Hf-O isotopes of detrital zircons from Hainan Island: Implications for Mesozoic subduction models. *Lithos* **2015**, *239*, 60–70. [[CrossRef](#)]
74. Faure, M.; Sun, Y.; Shu, L.; Monié, P.; Charvet, J. Extensional tectonics within a subduction-type orogen. The case study of the Wugongshan dome (Jiangxi Province, southeastern China). *Tectonophysics* **1996**, *263*, 77–106. [[CrossRef](#)]
75. Lin, W.; Faure, M.; Monie, P.; Scharer, U.; Zhang, L.S.; Sun, Y. Tectonics of SE China: New insights from the Lushan massif (Jiangxi Province). *Tectonics* **2000**, *19*, 852–871. [[CrossRef](#)]
76. Lin, W.; Ji, W.; Faure, M.; Wu, L.; Li, Q.; Shi, Y.; Scharer, U.; Wang, F.; Wang, Q. Early Cretaceous extensional reworking of the Triassic HP-UHP metamorphic orogen in Eastern China. *Tectonophysics* **2015**, *662*, 256–270. [[CrossRef](#)]
77. Zhu, G.; Xie, C.L.; Chen, W.; Xiang, B.W.; Hu, Z.Q. Evolution of the Hongzhen metamorphic core complex: Evidence for Early Cretaceous extension in the eastern Yangtze Craton, eastern China. *Geol. Soc. Am. Bull.* **2010**, *122*, 506–516. [[CrossRef](#)]
78. Li, J.; Zhang, Y.; Dong, S.; Su, J.; Li, Y.; Cui, J.; Shi, W. The Hengshan low-angle normal fault zone: Structural and geochronological constraints on the Late Mesozoic crustal extension in South China. *Tectonophysics* **2013**, *606*, 97–115. [[CrossRef](#)]
79. Ji, W.; Faure, M.; Lin, W.; Chen, Y.; Chu, Y.; Xue, Z. Multiple Emplacement and exhumation history of the Late Mesozoic Dayunshan-Mufushan Batholith in Southeast China and its tectonic significance: 1. Structural analysis and geochronological constraints. *J. Geophys. Res.* **2018**, *113*, 689–710. [[CrossRef](#)]
80. Dong, S.; Zhang, Y.; Zhang, F.; Cui, J.; Chen, X.; Zhang, S.; Miao, L.; Li, J.; Shi, W.; Li, Z.; et al. Late Jurassic–Early Cretaceous continental convergence and intracontinental orogenesis in East Asia: A synthesis of the Yanshan Revolution. *J. Asian Earth Sci.* **2015**, *114*, 750–770. [[CrossRef](#)]

81. Wang, W.; Zhou, M.F.; Yan, D.P.; Li, J.W. Depositional age, provenance, and tectonic setting of the Neoproterozoic Sibao Group, southeastern Yangtze Block, South China. *Precambrian Res.* **2012**, *192–195*, 107–124. [[CrossRef](#)]
82. Yan, D.P.; Zhou, M.F.; Song, H.L.; Wang, X.W.; Malpas, J. Origin and tectonic significance of a Mesozoic multi-layer over-thrust system within the Yangtze Block (South China). *Tectonophysics* **2003**, *361*, 239–254. [[CrossRef](#)]
83. Vollmer, F.W. Orient 3: A New Integrated Software Program for Orientation Data Analysis, Kinematic Analysis, Spherical Projections, and Schmidt Plots. *Geol. Soc. Am. Abstr. Programs* **2015**, *47*, 49.
84. Lloyd, G.E.; Freeman, B. Dynamic recrystallisation of quartz and quartzites. *J. Struct. Geol.* **1994**, *16*, 867–881. [[CrossRef](#)]
85. Stipp, M.; Stünitz, H.; Heilbronner, R.; Schmid, S.M. The eastern Tonale fault zone: A “natural laboratory” for crystal plastic deformation of quartz over a temperature range from 250 to 700 °C. *J. Struct. Geol.* **2002**, *24*, 1861–1884. [[CrossRef](#)]
86. Passchier, C.W.; Trouw, P.A.J. *Microtectonics*, 2nd ed.; Springer: Berlin, Germany, 2005.
87. Fossen, H. *Structural Geology*, 2nd ed.; Cambridge University Press: Cambridge, UK, 2016.
88. Xu, S.S.; Nieto–Amaniego, A.F.; Alaniz–Alvarez, S.A. Emplacement of pyroclastic dykes in Riedel shear fractures: An example from the Sierra de San Miguelito, central Mexico. *J. Volcanol. Geoth. Res.* **2013**, *250*, 1–8. [[CrossRef](#)]
89. Byerlee, J.D. Friction of rocks. *Pure Appl. Geophys.* **1978**, *116*, 615–626. [[CrossRef](#)]
90. Zhang, J.; Huang, W.T.; Wu, J.; Liang, H.Y.; Lin, S.P. Geological implications of apatite within the granite-related Jiepai W-(Cu) deposit, Guangxi, South China. *Ore Geol. Rev.* **2021**, *139*, 104548. [[CrossRef](#)]
91. Wang, Y.J.; Fan, W.M.; Sun, M.; Liang, X.Q.; Zhang, Y.H.; Peng, T.P. Geochronological, geochemical and geothermal constraints on petrogenesis of the Indosinian peraluminous granites in the South China Block: A case study in the Hunan Province. *Lithos* **2007**, *96*, 475–502. [[CrossRef](#)]
92. Ding, X.; Chen, P.R.; Chen, W.F.; Huang, H.Y.; Zhou, X.M. LA-ICPMS zircon U–Pb age determination of the Weishan granite in Hunan: Petrogenesis and significance. *Sci. China Earth Sci.* **2005**, *35*, 606–616.
93. Chen, W.F.; Chen, P.R.; Huang, H.Y.; Ding, X.; Sun, T. Chronological and geochemical studies of granite and enclave in Baimashan pluton, Hunan, South China. *Sci. China Earth Sci.* **2007**, *50*, 1606–1627. [[CrossRef](#)]
94. Li, Y.; Dong, S.W.; Zhang, Y.Q.; Li, J.H.; Su, J.B.; Han, B.F. Episodic Mesozoic constructional events of central South China: Constraints from lines of evidence of superimposed folds, fault kinematic analysis, and magma geochronology. *Int. Geol. Rev.* **2016**, *58*, 1076–1107. [[CrossRef](#)]
95. Xie, Y.H.; Gao, H.; Zhang, Z.; Yang, L.; Ke, X.X.; Liu, X.M.; Luo, J.B.; Liu, Q.; Xu, K.L.; Liu, J.S.; et al. Ore-forming fluid characteristics and material source of gold deposits in Tongdao County, Hunan Province, evidence from fluid inclusions and H-O-S isotopes. *Gold Sci. Technol.* **2021**, *28*, 74–88. (In Chinese with English abstract)
96. Gao, H.; Xie, Y.H.; Yang, L.; Zhang, Z.; Ke, X.X.; Liu, X.M.; Luo, J.B.; Liu, Q.; Liu, J.S.; Wang, Z.L.; et al. Composition typomorphic characteristics of pyrite and its genetic implication for gold deposits in Tongdao County, Hunan Province. *Gold Sci. Technol.* **2021**, *28*, 712–726. (In Chinese with English abstract)
97. Tian, E.N.; Wang, R.C.; Xie, L.; Zhang, W.L.; Che, X.D.; Zhang, R.Q. Mineralogy and geochemistry of the newly discovered Late Mesozoic granite-pegmatite and associated Sn-Nb-Ta-Be mineralization in the Miao’ershan-Yuechengling composite batholith, northern Guangxi, South China. *J. Asian Earth Sci.* **2020**, *190*, 104149. [[CrossRef](#)]
98. Wang, C.; Peng, J.T.; Xu, J.B.; Yang, J.H.; Hu, A.X.; Chen, X.J. Petrogenesis and metallogenetic effect of the Baimashan granitic complex in central Hunan, South China. *Acta Petrol. Sinica* **2021**, *37*, 805–829. (In Chinese with English abstract)